2026 IEEE International Conference on Robotics and Automation (ICRA 2026)
June 1-5, 2026. Vienna, Austria

Robotic Relay of Free-Space Optical Beams for Medical Applications

Guangshen Ma, PhD[1], Patrick Codd, MD[2] and Mark Draelos, MD, PhD[1,3]

***Abstract*— Medical robotic laser systems require high precision beam steering and sensor integration to support diverse applications, ranging from surgical intervention to optical tissue diagnostics. While conventional galvanometer-based mirror systems offer high-fidelity control, their fixed-base architecture limits their utility in procedures requiring broad coverage or large angular ranges, such as 360-degree full-view scanning. To expand imaging flexibility, we propose a novel robot-mirror framework to use robot-attached mirrors to control a 3D free-space laser beam, which is referred to as "N-mirror-N-robot system" where N is the number of mirrors and robots. This framework allows for general laser beam planning to trace 3D targets by using multiple robot-and-mirror combinations. We develop a prototype for the special case with a single mirror attached to the robot ($N = 1$). This prototype integrates an RGB-D depth camera for object tracking, a 6-DOF robot-attached mirror, and a laser diode source. We propose a computational framework for system kinematics and calibration. Simulation and real experiments are conducted to track specified paths, markers, phantoms, and real tissue to verify the system feasibility. The results show an average object tracking error of approximately 2.0 mm that is close to the depth accuracy of the camera. This $N = 1$ prototype shows promise for $N > 1$ case and the potential for general 3D laser planning under arbitrary geometric constraints.**

I. Introduction

In medical robotics, laser systems have been widely used as surgical scalpels in various medical applications such as eye surgery [1], [2], neurosurgery [3], [4], dermatology [5] and volumetric tissue removal [4]. Lasers can also be used in the design and construction of optical sensors, such as fluorescence spectroscopy [6] (using a laser diode to facilitate the examination of molecular structures) and non-contact surface profiling with 3D laser triangulation sensors [7]. These platforms have been commonly used for specialized medical applications, including optical microscope designs with multiple galvo-based mirrors [8] and the development of robotic optical coherence tomography (OCT) [9]. Combining mirrors and robots for system development is important for accurate laser beam control, where existing platforms are commonly categorized according to degree-of-freedom (DOF) and the scanning workspace of the robot manipulator: 1) robot-controlled and 2) mirror-controlled methods.

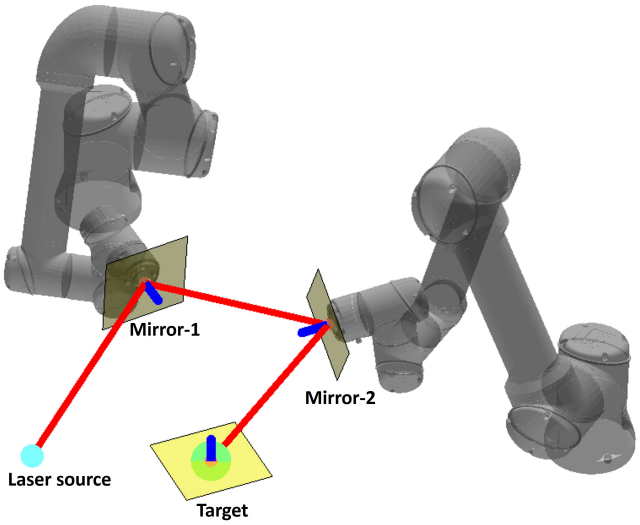

Fig. 1: N-robot-N-mirror ($N = 2$) system. Compared with $N = 1$, adding a second robot-mirror sub-system enables the laser beam to visit an expanded scanning region.

1) Robot-controlled laser model: The robot-controlled method adjusts the position and orientation of a laser aperture or a fiber-coupled laser directly by attaching a laser to the robot end-effector (EE), such as a robot arm [5], [10], a concentric tube robot [11], [12], an endoscopic robotic laser system [13], or a cable-driven parallel mechanism [14]. These robot-laser configurations rely solely on the robot manipulator to direct the laser beam (as an output from the robot-EE) in different 3D surgical scenes, where the flexibility and dexterity are limited by the degrees of freedom of the robot. Even with the laser-based sensor system attached to the robot-EE (e.g., the robot OCT system [9], the laser-induced fluorescence system [6], [3]), the robot-controlled laser system (attached to robot-EE) cannot reach all the possible 3D regions (e.g., 360 full-view scanning) due to the limited workspace of a single robot arm setting. This lack of scanning flexibility limits the laser usage in scanning large-area tissue regions and in avoiding 3D obstacles that can block the laser beams towards the targets.

2) Mirror-controlled laser model: An alternative method is to attach a small steering mirror system (e.g., a galvanometer) on the robot end-effector to improve the system flexibility [15]. This approach offers significant advantages in laser control due to steering mirrors' high-speed and high-

[1]GM and MD are with the Department of Robotics, University of Michigan, Ann Arbor, MI USA (email: guangshe@umich.edu).
[2]PC is with the Dept of Neurosurgery and Dept of Mechanical Engineering and Materials Science, Duke University, Durham NC 27705, USA.
[3]MD is also with the Department of Ophthalmology and Visual Sciences, University of Michigan Medical School, Ann Arbor, MI USA.
This work was supported by the National Institute of Biomedical Imaging and Bioengineering and the Office of the Director of the National Institutes of Health under award number DP2 EB039104 and by the University of Michigan. The content is solely the responsibility of the authors and does not necessarily represent the official views of the National Institutes of Health.

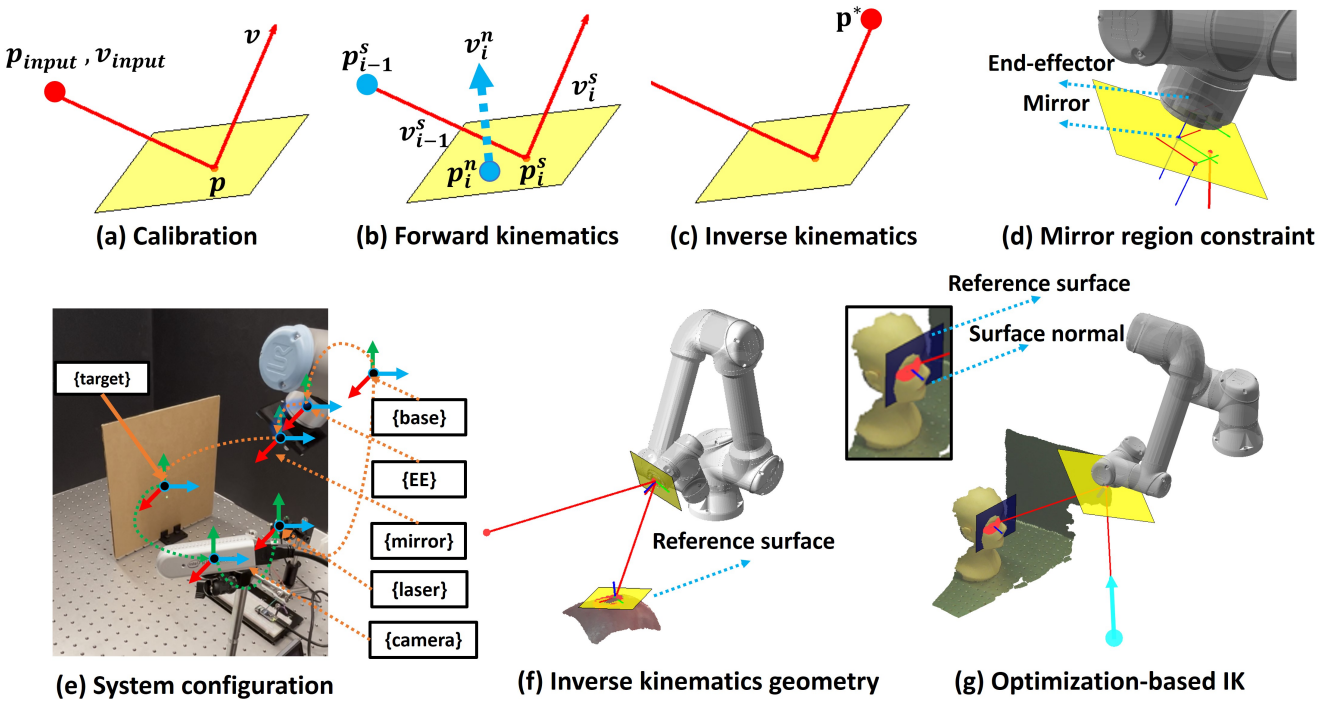

Fig. 2: System layouts and geometry. (a) System calibration aims to estimate the optimal laser orientation and position as inputs to the system through free-space propagation to the target positions. (b,c) The forward and inverse kinematics model describes the relationship among the mirror, robot configurations, laser positions and orientations. (d) The mirror geometry where the laser beam point of incidence should be located within the reflection region. (e) The system setup to fit a local reference plane (with position and orientation of the mirror) at the target planar surface, with the RGB-D camera and the robot-to-mirror configuration. (f, g): Examples of using target reference planes (fitting with singular value decomposition) to formulate the inverse kinematics model, which estimates the optimal robot-mirror configuration for laser beam control.

precision capabilities. These mechanisms have been applied in the variety of tabletop optical systems for microscopes, OCT sensor development [15], fluorescence sensor design [6], robotic laser surgery [16], [17], [18], and optical imaging system design [19], [20]. Despite the coarse and fine adjustments to control the laser beam using the robot and mirror, respectively, the scanning capability to achieve a complete scan is still limited by the constrained robot workspace.

3) N-mirror-N-robot framework: Addressing the limitations of conventional galvo-controlled and robot-mounted laser models, we explore a novel method that uses multiple robot-mirror systems to avoid scanning limitations, which is referred to as the "*N*-mirror-*N*-robot platform." By employing a robot-controlled multi-mirrors architecture, this approach effectively resolves the field-of-view constraints that typically limit the efficacy of independent galvo-steering and fixed robot-mounted laser systems. This framework with an arbitrary number of mirrors for laser steering has not previously been addressed in the fields of robotics, lasers, and optics. Solving this problem can be beneficial for design of multi-mirror systems for complicated surgical applications, which provides a generalized framework for navigating, focusing, and manipulating laser beams or laser-based sensors along complex and constrained anatomical pathways [15]. By combining laser steering with extra laser modules (e.g., 3D laser-based distance sensors or laser scalpels), the system can enable precise, non-contact, and multi-sensor guided procedures in space-restricted environments such as transoral laser microsurgery or ophthalmic surgery [21], [22].

The development of the proposed multi-robot-mirror system requires understanding of light propagation in 3D. Ray optics, or geometric optics, offers a simplified, yet powerful way to understand the behaviors of light as it interacts with surfaces and travels through different media [23]. However, the modeling of geometric optics and robotic systems has not been addressed and leaves open research questions. This motivates the proposed research to focus on the development of a novel optics-robot algorithm framework to study the relationship of mirrors and robot manipulation in free space.

As a preliminary study for the *N*-mirror-*N*-robot platform, we first demonstrate feasibility with a simplified system incorporating a single mirror attached to one robot arm (i.e., $N = 1$). This laser-based surgical system can be considered as a robot platform with forward and inverse kinematic models, and is different from existing optical systems consisting of multiple fixed mirrors to transmit the laser beam to the target surface [24], [25], [26]. We summarize our contributions as:

1) ***N*-mirror-*N*-robot algorithm framework ($N = 1$):** We develop a novel *N*-mirror-*N*-robot framework and

demonstrate the $N = 1$ case with a depth camera and a robot-attached mirror to control the laser beam.

2) **System calibration**: We develop a general calibration method to estimate the configurations of the laser inputs, camera positions, and the robot-attached mirror geometry, which allows for accurate 3D laser tracking.
3) **Kinematics modeling**: We develop a forward and inverse kinematics framework to estimate the optimal robot-mirror configurations for laser beam steering.

II. METHODS

A. System Model

We first demonstrate the *N*-mirror-*N*-robot system with a special case ($N = 1$). This system incorporates a single mirror ($75mm \times 75mm$ flat mirror, Edmund Optics) attached to the 6-DOF robot end-effector (UR5e, Universal Robots Inc.). The laser (red laser diode: 650 nm wavelength, Quarton Inc.) starts from a fixed origin with vector configuration, and the laser beam propagates to reach a 3D target. The target can be tracked by the RGB-D camera (Intel RealSense D435) using the real-time point cloud reconstruction from depth images. For system modeling, we define the world frame at the base of the robot as T_{base}. The depth camera frame is defined as T^{base}_{camera} relative to the robot base. The mirror frame is defined in the pivot center with the perpendicular orientation vector as T^{mirror}_{base}. The system configuration is shown in Fig. 2e.

B. Forward Kinematics

We first revisit the geometry of the laser-mirror model [27], [28] and discuss how this model can be used to derive the kinematics of a single-mirror robot system. The kinematics model defined in this study is different from the conventional robot kinematics model. The proposed kinematics model studies the motion of the laser controlled by the robot-mirror configuration. We first derive the mapping function between a single laser input and a reflection mirror for the case of $N = 1$, and we can show that the same method can be extended to the general N-mirror cases (Fig. 2a-c).

For a single laser-mirror model between the $(i-1)$-th laser input and the i-th mirror (Fig. 2a-c), the 5-DOF laser input (no roll due to symmetry) is denoted by the laser position $\mathbf{p}^s_{i-1} \in \mathbb{R}^3$ and direction vector $\mathbf{v}^s_{i-1} \in \mathbb{R}^3$. A rotary mirror configuration can be uniquely defined by the center of the mirror $\mathbf{p}^n_i \in \mathbb{R}^3$ and the normal vector of the mirror $\mathbf{v}^n_i \in \mathbb{R}^3$. The laser output after beam reflection can be denoted as the laser position $\mathbf{p}^s_i \in \mathbb{R}^3$ and orientation $\mathbf{v}^s_i \in \mathbb{R}^3$. Therefore, the configuration of $\mathbf{p}^s_{i-1}, \mathbf{v}^s_{i-1}, \mathbf{p}^n_i, \mathbf{v}^n_i, \mathbf{p}^s_i, \mathbf{v}^s_i$ formulates a unique robot system with the full kinematic model. To compute $\mathbf{p}^s_i$, we have the laser reflection model from [27], [28] ("$\cdot$": dot product):

$$\mathbf{p}^s_i = \mathbf{p}^s_{i-1} - \frac{\mathbf{v}^n_i \cdot (\mathbf{p}^s_{i-1} - \mathbf{p}^n_i)}{\mathbf{v}^n_i \cdot \mathbf{v}^s_{i-1}} \mathbf{v}^s_{i-1} \tag{1}$$

For the laser output vector $\mathbf{v}^s_i$, we have [27], [28]:

$$\mathbf{v}^s_i = \mathbf{v}^s_{i-1} - 2\ (\mathbf{v}^s_{i-1} \cdot \mathbf{v}^n_i)\ \mathbf{v}^n_i \tag{2}$$

The laser inputs and outputs are all defined in the robot base frame. Next, we define the geometric relation between the mirror and the robot. Given T^{EE}_{base}, T^{mirror}_{EE}, and $T^{i}_{EE}(\mathbf{q})$ ($\mathbf{q} \in \mathbb{R}^6$ is the robot configuration), the mirror transformation is $T^{mirror}_{base} = T^{EE}_{base}\ T^{mirror}_{EE}$. where T^{mirror}_{base} can be defined as the case $T^{mirror}_{base} = [[v^T_x, 0], [v^T_y, 0], [v^T_z, 0], [p^T_z, 1]]_{4\times4}$. We define v^T_z as the surface normal vector of the mirror. We denote the variable $\mathbf{X} = T^{mirror}_{EE} \in \mathrm{SE}(3)$ that encodes the orientation and translation between the robot-EE and the mirror.

Starting from the laser input to the target point (i.e., the point is captured by camera and transformed into the robot base frame), we describe the laser-mirror intersection point as $\mathbf{p}^s_i = f_{point}(\ T^{base}_{camera},\ T^{EE}_{base}(\mathbf{q}),\ T^{mirror}_{EE}\ )$. For orientation, we have $\mathbf{v}^s_i = f_{vector}(\ T^{base}_{camera},\ T^{EE}_{base}(\mathbf{q}),\ T^{mirror}_{EE})$. Here, T^{base}_{camera} and T^{mirror}_{EE} are obtained by system calibration. The target point is used to defined $\mathbf{p}^{camera}$ (homogeneous vector) that is transformed into the base frame as $T^{base}_{camera}\mathbf{p}^{camera}$.

Reference mirror to the target point: As a laser ray can reach the target point with different incident orientations, we need to define a local reference frame based on the target point such that only one unique point can be intersected with the surface. Thus, we assign a virtual mirror (reference plane) to each target point, and this additional reference plane can be considered as the $(N+1)$-th mirror. The "predicted point" is defined as the point where the laser beam from the last mirror intersects with the virtual mirror.

Summary of the FK model: In summary, we can describe the entire forward kinematics model as follows:

$$\mathbf{p}^s_{i=t} = f_{point}(\underbrace{\mathbf{X}}_{T^{base}_{camera}},\ \underbrace{\mathbf{Y}}_{T^{mirror}_{EE}},\ \underbrace{\{\mathbf{p}^s_{i=0}, \mathbf{v}^s_{i=0}\}}_{\text{laser input}}, \underbrace{\{\mathbf{p}^n_i, \mathbf{v}^n_i\}|^{i=t}_{i=1}}_{\text{mirror-config}}) \tag{3}$$

For the laser orientation, we have:

$$\mathbf{v}^s_{i=t} = f_{vector}(\underbrace{\mathbf{X}}_{T^{base}_{camera}},\ \underbrace{\mathbf{Y}}_{T^{mirror}_{EE}},\ \underbrace{\{\mathbf{p}^s_{i=0}, \mathbf{v}^s_{i=0}\}}_{\text{laser input}}, \underbrace{\{\mathbf{p}^n_i, \mathbf{v}^n_i\}|^{i=t}_{i=1}}_{\text{mirror-config}}) \tag{4}$$

Here, $\mathbf{X} = T^{base}_{camera} \in \mathrm{SE}(3)$ and $\mathbf{Y} = T^{base}_{camera} \in \mathrm{SE}(3)$ are the system parameters to be calibrated. The $\{\mathbf{p}^s_{i=0}, \mathbf{v}^s_{i=0}\}$ are decoded from $T_{laser} \in \mathrm{SE}(3)$ as the origin and Z-axis vector of the transformation matrix. The $\{\mathbf{p}^n_i, \mathbf{v}^n_i\}|^{i=t}_{i=1}$ represent the mirror configurations from $i = 1$ to $i = t$, where t is the ID of the mirror defined at the target point. This model describes the mapping from the laser input to the intersection point and the reflection vector of the 3D target.

C. Inverse Kinematics

The inverse kinematics (IK) problem aims to estimate the optimal mirror configurations so that the predicted laser path can match the given targets. In this study, we redefine the IK problem and formulate the optimization-based solver by using the cost function between the predicted point (of the target) and the true one measured in the camera.

1) Initial robot-mirror configuration: As a small change of the mirror orientation can contribute to a large laser incidence offset to the target point, we define an initial robot-mirror configuration $T^{base}_{EE-first} \in \mathrm{SE}(3)$ to always place the

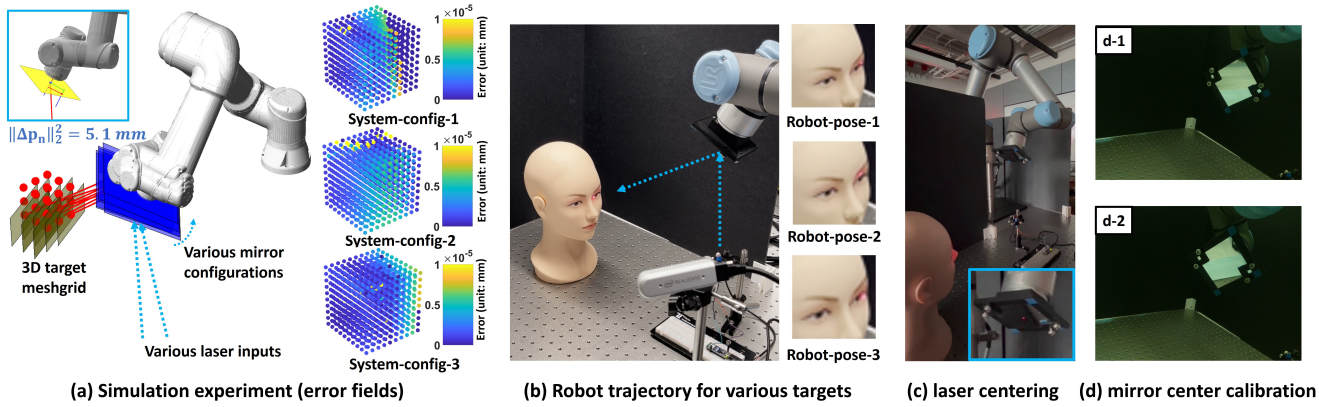

Fig. 3: (a) Sample system configurations with randomized mirror-to-EE transformations and laser source positions. To test generalization, laser and robot-to-mirror parameters were varied per trial while target 3D meshgrids remained fixed (overlaid error map). Each target is paired with an optimized robot configuration for precise beam control. (b) An example of the robot-mirror configurations for various laser targets (red spot). (c) A visualization of the laser beam centering around the mirror. (d) Two poses of the calibration method to estimate the realistic mirror center (fiducial markers at the mount corners).

laser in the feasible region (in the mirror ROI). To minimize the target-to-initial pose deviation, we propose an adjusted IK formulation:

$$T_{mirror}^{base} = T_{EE-first}^{base}(\mathbf{q})\ (T_{mirror}^{EE}\ \mathbf{\Delta Y}) \tag{5}$$

where $\mathbf{\Delta Y} = \Delta T_{mirror}^{EE} \in \mathrm{SE}(3)$ is the output of the proposed IK solver. This transformation offset enables the laser beam to always be localized in the feasible mirror region. Given T_{mirror}^{EE} and T_{camera}^{base} from the system calibration, we revisit the FK model with $\Delta\mathbf{Y}$ for $f_{point}(\cdot)$ as:

$$\mathbf{p}_{i=t}^{s} = f_{point}(\ \underbrace{\Delta T_{mirror}^{EE}}_{\text{mirror offset}},\ \underbrace{\{\mathbf{p}_{i=0}^{s},\ \mathbf{v}_{i=0}^{s}\}}_{\text{laser input}},\ \underbrace{\{\mathbf{p}_{i}^{n}, \mathbf{v}_{i}^{n}\}|_{i=1}^{i=t}}_{\text{mirror-config}}\ ) \tag{6}$$

2) Optimization for inverse kinematics (IK): We develop an optimization-based IK solver to estimate the optimal mirror configuration for laser beam steering. The target points on the tissue surface are defined as $\{\overline{\mathbf{q}}_j\}_{j=1}^{M}$, $\overline{\mathbf{q}}_j \in \mathbb{R}^3$. The list of variables can be defined as $\mathbf{w}_j = \{{p_j}^n, {v_j}^n\}_{j=1}^{m}$ where each combination of $\{{p_j}^n, {v_j}^n\}$ denotes the mirror configuration. The IK solver aims to calculate the optimal mirror positions and orientations by minimizing the sum-of-squares costs between the predicted and target points. Rotation angles and translation vectors are used to describe the transformation matrix and we define the variable as $\mathbf{w}_j = [\theta_x, \theta_y, \theta_z, x, y, z] \in \mathbb{R}^6$. The IK is modeled as:

$$\min_{\Delta T_{EE}^{mirror}} \sum_{j=1}^{M} \underbrace{||\ f_{point}^{i=t}(\cdot) - \overline{\mathbf{p}}_j^{s}\ ||_2^2}_{g(\cdot)\text{: j-th point target cost}} + \underbrace{||\ f_{point}^{i=t-1}(\cdot) - \mathbf{p}_i^{n}\ ||_2^2}_{h(\cdot)\text{: laser-to-mirror center cost}} \tag{7}$$

where we define $\mathbf{p}_j^t = f_{point}^{i=t}(\Delta T_{EE}^{mirror}, T_{EE}^{mirror},\ T_{i=0}^{laser})$, $\mathbf{p}_n^{t-1} = f_{point}^{i=t-1}(\Delta T_{EE}^{mirror}, T_{EE}^{mirror},\ T_{i=0}^{laser})$. The settings of [-60, +60] × [-60, +60] degrees for rotations (X and Y axes) and [-0.05, +0.05] meters for translation were used in the IK solver. The $g(\cdot)$ and $h(\cdot)$ represent the cost items in the objective function. The analytical Jacobian matrix is described as $J(\mathbf{\Delta w}) := [\ \frac{\partial g(\cdot)}{\partial \mathbf{\Delta w}}, \frac{\partial h(\cdot)}{\partial \mathbf{\Delta w}}]$ and we have $\Delta\mathbf{w} = [\Delta\theta_x, \Delta\theta_y, \Delta\theta_z, \Delta p_x, \Delta p_y, \Delta p_z]$ as rotation angles and translation vectors to describe ΔT_{EE}^{mirror} in the cost function. Notably, we incorporate a "mirror center cost item" into the cost function to ensure the laser beam remains near the geometric center of the mirror to prevent the loss of reflection. Even with 3D obstacles, the laser beam can be planned around the mirror center by adjusting the geometric constraints or objective functions in the cost function.

D. System calibration

1) RGB-D camera calibration: We applied the conventional hand-eye calibration method to estimate the transformation of the RGB-D camera to the base frame of the robot T_{camera}^{base}. To simplify the procedure, we used a three-marker calibration board to directly use the 3D sphere markers of the chessboard pattern to formulate the objective function.

$$\begin{aligned} E_j &= f_j^{camera}(\ T_{camera}^{EE},\ T_{marker}^{base}\ ;\ T_{EE}^{base}(\mathbf{q}_j)\ ) \\ &= ||\ T_{EE}^{base}(\mathbf{q}_j)\ T_{camera}^{EE}\ p_i^{camera} - T_{marker}^{base}\ p_i^{marker}||_2^2 \end{aligned} \tag{8}$$

Here p_i^{camera} and p_i^{marker} are homogeneous vectors. Therefore, the objective function $f_k^{camera}(\cdot)$ is formulated as a variant of the conventional robot hand-eye calibration [29]:

$$\min_{\mathbf{X},\ T_{marker}^{base}} \sum_{k} f_k^{camera}(\ \mathbf{X} = T_{camera}^{base},\ T_{marker}^{base}\ ) \tag{9}$$

where k is the ID of the calibration pose and T_{camera}^{base} describes the camera-to-base transformation. T_{marker}^{base} denotes the base-to-marker (marker frame) transformation.

2) Laser origin and mirror geometry calibration: system calibration aims to determine the 5-DOF laser input and the 5-DOF mirror-to-robot transformation. We formulated the system calibration as a nonlinear least-squares minimization problem that aims to penalize the point-based error items between the predicted points and the 3D fiducial markers. We used a planar calibration board to formulate geometric

constraints of the cost function and placed the board in different spatial positions. For each position, the robot-mirror performed a discrete scan with multiple points based on a predefined path. The corresponding robot configurations (for the mirror) were recorded when the laser was incident on the fiducial position. Each scan corresponded to a unique laser spot and its 3D position. The optimal laser input is expected to achieve the minimal point-based errors between the predicted point and the 3D target fiducial. We define $\{\hat{\mathbf{p}}_j\}_{j=1}^{M}$, $\hat{\mathbf{p}}_j \in \mathbb{R}^3$ as the 3D fiducial markers and the optimization problem can be formulated:

$$\min_{\mathbf{Y};\ \mathbf{p}^s_{i=0},\mathbf{v}^s_{i=0}} \quad \sum_{j=1}^{M} \| f^{i=j}_{point}(\ \mathbf{Y},\ \underbrace{\{\mathbf{p}^s_{i=0},\mathbf{v}^s_{i=0}\}}_{\text{from } \mathbf{T}_{\mathbf{laser}}}\ ) - \underbrace{\hat{\mathbf{p}}_j}_{\text{calib}} \|_2^2 \tag{10}$$

Where we have $\mathbf{p}^t_j = f^{i=j}_{point}(\mathbf{Y},\ \{\mathbf{p}^s_{i=0},\mathbf{v}^s_{i=0}\})$ and $\mathbf{Y} = T^{mirror}_{EE}$. The $\mathbf{p}^s_{i=0}$ is the origin and $\mathbf{v}^s_{i=0}$ is the Z-axis vector of $T^{laser}_{i=0}$. We can add the derivative of the cost function with respect to $\mathbf{p}^s_{i=0}$ and $\mathbf{v}^s_{i=0}$ to the MATLAB nonlinear optimization solver ("Levenberg-Marquardt" method) for the solution. Solving this optimization enables the estimations of the laser origin and the mirror configuration (Fig. 3a).

III. Simulation Experiments

We conducted a simulation study to evaluate the one-mirror-one-robot system to target arbitrary 3D markers in various configurations (Fig. 3a). A 1000-point cubic grid ($100 \times 100 \times 100\ mm^3$) served as the workspace for the inverse kinematics (IK) targets. To evaluate system robustness, we introduced perturbations to the laser inputs and the mirror-effector transformation matrix, as derived from realistic calibration data, to simulate hardware misalignments and mounting variations. Stochastic perturbations were applied to the transformation matrices for both the IK and the calibration solvers. These offsets were sampled from a uniform distribution $\mathcal{U}(-1,1)$ and scaled by a factor of $\theta = [5°, 5°, 5°]^T$ for orientation and $\mathbf{p} = [10, 10, 10]^T$ mm for translation. These parameters covered most medical scenarios with robot laser systems [30].

1) Inverse kinematics testing: We first conducted a simulation experiment to verify the feasibility of the optimization-based IK solver in Eq. 7. The perturbed laser inputs and the mirror-to-EE transformations served as various system settings. The IK solvers (Eq. 7) were implemented with an orientation constraint of $[-90, +90]$ degrees and a distance constraint of $[-0.10, +0.10]$ meters. The orientation angles and translation vectors were used to describe the rigid transformation matrix as inputs for the system to test the IK solver. We conducted ten repeat tests and the examples of 3D error maps are shown in Fig. 3a. The majority of the target errors were smaller than 10^{-5} mm (with maximum error smaller than 5×10^{-4} mm).

2) Calibration testing: Simulation experiments were conducted with 100 repeated tests to verify the calibration algorithm in Eq. 10. For each trial, a randomized combination of the variables was used as system input (true targets), including the laser position and orientation and the initialized pose of the robot-mirror (position and orientation). The solvers were implemented with an orientation range of $[-360, +360]$ degrees and a distance range of $[-10, +10]$ meters. For each case, we compared the position and orientation offsets of the laser input and the mirror-to-EE transformation to the true targets. The simulation results showed that the maximum positions are smaller than 10^{-5} mm and the orientation offsets smaller than 10^{-6} degrees.

3) Sensitivity analysis: To evaluate the robustness of the inverse kinematics (IK) solver against calibration inaccuracies in simulation, we conducted a sensitivity analysis by perturbing the laser and mirror configurations (Fig. 4). We introduced stochastic noise to the calibrated transformation matrices using the following perturbation model with $\boldsymbol{\theta}_{real} = \boldsymbol{\theta}_{raw} + \boldsymbol{\sigma} \cdot \Delta\boldsymbol{\theta}$ and $\boldsymbol{p}_{real} = \boldsymbol{p}_{raw} + \boldsymbol{\lambda} \cdot \Delta\boldsymbol{p}$, where components of $\boldsymbol{\sigma}$ and $\boldsymbol{\lambda}$ were sampled from a uniform distribution of $\mathcal{U}(-1,1)$. We evaluated three discrete perturbation levels of $\Delta\theta \in \{0.25°, 0.50°, 1.00°\}$ and $\Delta p \in \{2.5, 5.0, 10.0\}$ mm. For each level, the IK solver was evaluated using 64 targets sampled uniformly from a $20 \times 20 \times 20\ cm^3$ workspace. To ensure statistical significance, each perturbation was repeated 10 trials with randomized scaling factors. System performance was quantified using the 3D target error, comparing perturbed IK solutions against the nominal calibrated model.

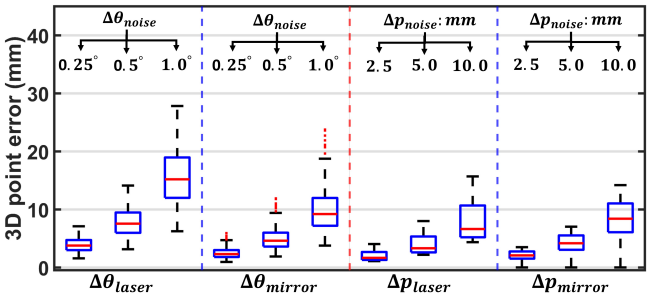

Fig. 4: Sensitivity analysis for system calibration ($\Delta\theta = 0.25, 0.5, 1.0$, unit: degrees; $\Delta p = 2.5, 5.0, 10.0$ mm). Each section shows the results of three levels of changes. The 3D error shows how the changes of the system inputs affect the output performance of the IK solver. The $\Delta\theta_{laser}$, Δp_{laser}, $\Delta\theta_{mirror}$ and Δp_{mirror} indicate the changes of laser input orientation (described by angles), laser input positions, mirror orientation (described by angles) and mirror center positions. The $\Delta\theta$ and Δp show various noise levels.

The results in Fig. 4 demonstrate that the target error is primarily sensitive to orientation stability, with minor angular deviations causing more performance degradation than positional shifts. Furthermore, the monotonic increase in error variance relative to perturbation scale suggests that orientation and position inaccuracies exhibit spatially varying influences across the 3D workspace. This behavior is expected, as the impact of a specific offset is configuration-dependent. For example, angular errors can be amplified by the beam's propagation distance, leading to higher sensitivity at certain target locations.

We further conducted a sensitivity analysis to isolate the impact of mirror configuration inaccuracies on the IK solver (Fig. 5). Orientation perturbations were applied within a range of $[-1, +1]^\circ$ with a 0.2° step size, while positional offsets ranged from $[-10, +10]$ mm with a 2.0 mm step size. The results demonstrate that the system is significantly more sensitive to rotational deviations compared to translational offsets. This can be attributable to the fact that positional error on a target increases as the beam travels further. Furthermore, the higher error variance observed with orientation changes suggests that minor angular fluctuations in the mirror lead to disproportionately large 3D target errors.

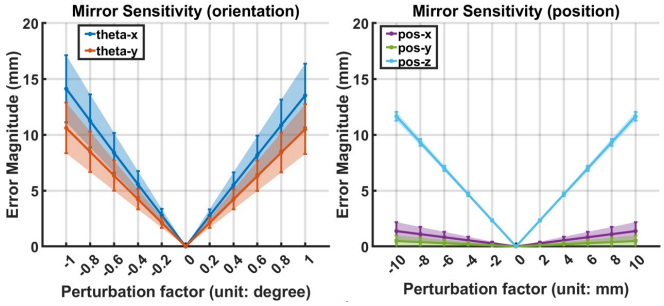

Fig. 5: Overview of sensitivity analysis for the changes of the mirror configuration (orientation and position offsets).

IV. Realistic Experiments

A. System calibration

1) Camera-to-robot transformation: We solved the proposed Eq. 9 with the MATLAB optimization solver ("Levenberg-Marquardt" method). We selected 20 different robot configurations to cover the variety of orientation and translation for the calibration targets. The average 3D reprojection errors are reported as 1.13 ± 0.50 mm.

2) Laser input and mirror-to-robot transformation: For the actual implementation, we randomly generated 16 robot poses to move the laser beam towards different orientations and translations. The calibration board was placed at three different positions, in which the same robot poses were applied to collect the datasets of 3D laser spots and robot configurations. This improves the calibration accuracy by minimizing the possibilities of getting incorrect laser orientations that can match to the same spots (Fig. 6a). In summary, the average 3D reprojection errors of all three groups of data were reported as 2.04 ± 1.25 mm. The statistics indicate that there are no significant differences between the errors of different placements of the calibration boards. This shows the consistency of the proposed algorithm in tracing a 3D point across various positions in the 3D space.

3) Mirror center estimation: As at the mirror surface, multiple pivot points can be used to define a planar surface in 3D space, and we thus need to verify the calibrated mirror center aligns with the realistic one. We provided another calibration procedure (solving Eq. 9) with four fiducial markers attached to the corners of the mirror mount to estimate the realistic mirror center. We calculated the center offset between the estimated result and the calibrated one is provided in Eq. 10. The 3D distance between the estimated and calibrated mirror centers was reported as 5.1 mm. This constitutes 6.8% ($< 10\%$) of the mirror length (i.e., 75 mm for the rectangular mirror length). When solving Eq. 7, this small offset would not contribute to the large deviation of the laser spot on the mirror ROI. Thus, we used the calibrated mirror center from Eq. 10 to perform the experiment.

B. Comprehensive target tracking experiments

We conducted comprehensive experiments that covered the targets of fiducial markers, trajectories, face phantom, and realistic finger objects. The average speed of the proposed IK solver (Eq. 7) was reported as 0.020 ± 0.022 seconds. For statistical analysis, we applied the independent two-sample t-test to analyze the average values between compared groups.

Experiment-1: Chessboard marker tracking. We performed a standardized chessboard marker tracking experiment to characterize the accuracy of the system. The goal was to segment the 3D fiducial markers of the chessboard with three different placements, and the IK solvers were used to estimate robot trajectories for visiting all these targets. The average errors for the entire dataset were reported as 1.61 ± 0.77 mm, and the statistical results (Fig. 6b) indicate that there are no significant differences between various locations on the chessboard.

Experiment-2: Trajectory following. We conducted another standardized trajectory tracking experiment and used the target board with a "curve path" to mimic realistic cases of vessel following for medical applications. The path was segmented and manually selected from the reconstructed pointcloud (as targets) to generate discrete 3D targets, and the IK solver was implemented to estimate the optimal path to visit the points. The statistics of the 3D point-to-point (closest point) error between the predicted and the gold standard are reported in Fig. 6c. For two combinations of position comparisons, there is a significant difference ($p < 0.001$) with one exception case that shows no significant difference. The average errors for the entire dataset was reported as 3.61 ± 1.58 mm.

Experiment-3: Phantom surface tracking. This experiment aims to demonstrate the system's capability in tracing the points in surfaces with arbitrary geometry. We conducted the experiment based on a human face phantom. Randomized trajectories were manually selected as 3D targets around the eyebrow regions, and the IK solver was used to estimate the optimal robot trajectory to visit these points. The average errors of the entire dataset were reported as 3.29 ± 1.72 mm. The statistics of the 3D point-to-point error (with correspondences) between the predicted and the gold standard are reported in Fig. 6d. Similarly to the performance of the path tracing task, there is one case that shows no significant difference, while for the other two cases, they show a significant difference ($p < 0.001$).

Experiment-4: Finger surface tracking. The finger surface tracking experiment aims to demonstrate the system's capability in tracing the points in a realistic tissue surface. With a finger target randomly placed in the workspace,

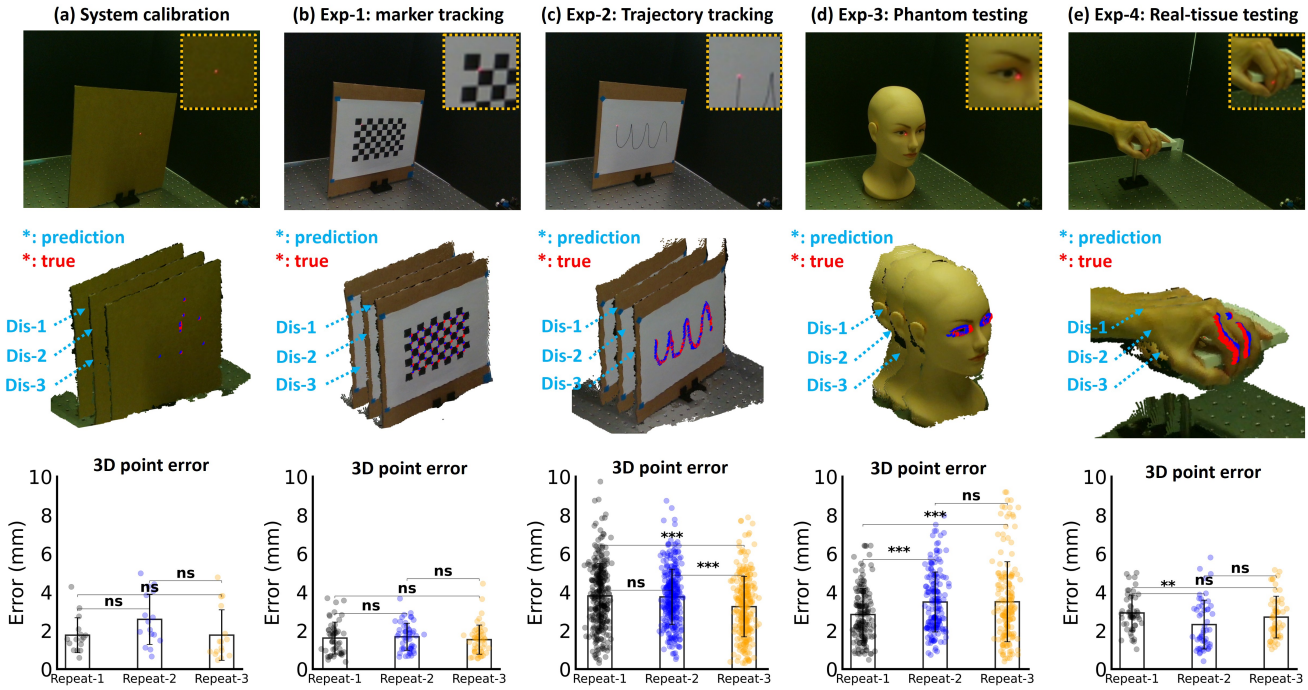

Fig. 6: Overview of realistic experiments. The first row shows 2D reference images. The second row show colorized pointcloud (with overlapped laser spots). The third row show the barchart of the 3D point-to-point errors. (a) System calibration verification. (b) Marker tracking experiment. (c) Trajectory tracking experiment. (d) Face phantom experiment. (e) Finger tissue experiment. Statistical index: $* : p < 0.05$, $** : p < 0.01$, $*** : p < 0.001$, ns: not significant.

the operator manually selected the trajectory on the finger surface using the colorized point cloud information. The IK solver was used to estimate the optimal path of the robot to visit these points. The average 3D point-to-point errors (with correspondences) between the predicted and true targets of the entire dataset were 2.65 ± 1.13 mm (Fig. 6e). In addition to one case showing a significant difference ($p < 0.01$), the other two cases show no significant difference.

V. Discussions and Conclusions

In this study, we presented a novel robot-mirror algorithm framework for laser beam steering using an arbitrary number of robot-mirror configurations. We characterized the preliminary system configuration that comprises a single laser source, a mirror-integrated 6-DOF robotic arm, and a target point, based on the simulation and realistic experiments.

In simulation, the calibration framework achieved a maximum position error of 10^{-5} mm and an orientation offset of 10^{-6} degrees across all test cases. In addition, the IK solver demonstrated high numerical precision with target errors typically below 10^{-5} mm. The maximum error remains under 5×10^{-4} mm, with minor fluctuations likely stemming from numerical instability or geometric sensitivity. These results confirm the system's consistency and its feasibility for tracking targets of arbitrary geometries. However, certain limitations remain for this preliminary study. From the sensitivity analysis in the simulation, the discrepancy of the laser tracing error across various studies shows that the current system is sensitive to the accuracy of the 3D reconstruction from the current 3D camera, the system calibration for the mirror-to-robot transformation, and the laser-to-base transformation. A closed-loop tracking algorithm may help in minimizing these 3D errors when the trajectory has to be continuous. The current lack of closed-loop capability limits the system in minimizing the error offsets between the predicted and the target ones, which could be addressed by implementing a visual servo algorithm to dynamically adjust the laser beam onto the intended targets. Although with great potential for real-time object tracking, the current system has not been shown to track dynamic objects with a fast update frequency. Future works can focus on the development of fast object tracking algorithms and improvements of the IK solver to accelerate the optimization procedure.

For realistic experiments, the reprojection errors for the system calibration show average errors of 1.13 ± 0.50 mm (camera-to-robot) and 2.04 ± 1.25 mm (mirror-to-robot and laser-to-robot), respectively, for various robot poses. The performance of our proposed system was limited by the accuracy of the RGB-D camera in 3D reconstruction (the depth reconstruction can be affected by the lighting conditions and the errors towards various depths). In addition, the chessboard marker experiment with an average error of 1.61 ± 0.77 mm was consistent with this.

The path tracing and face phantom experiments show higher error levels compared to the marker tracking study (3.61 ± 1.58 mm and 3.29 ± 1.72 mm). The instability and reduced accuracy of the RGB-D cameras in various

depths can contribute to this error discrepancy. Additionally, a small orientation offset of the laser beam can contribute to a large positioning error for large object distances. Future works can focus on collecting more data points to improve the calibration and produce more reliable results from our proposed optimization solver. As a demonstration, we also performed a realistic tissue study to trace human fingers with manual labeled targets. This verifies that our system can be adapted to various real-tissue models with arbitrary 3D sensors (e.g., 3D stereovision or 3D structure light sensors).

The proposed N-mirror-N-robot system can be widely applied in various fields including robotic laser surgery, free-space optical power transmission, 3D sensor development, and 3D free-space scanning. From the modeling perspective, this approach provides novel insights into general laser-based optics and robot system development regarding the challenges of free-space laser propagation. Moreover, the proposed system shows potential to trace 3D tissue models (e.g., tumor and vascular structures) for biomedical and clinical research in surgical robotics and robotic laser surgery.

REFERENCES

[1] R. Channa, I. Iordachita, and J. T. Handa, "Robotic eye surgery," *Retina (Philadelphia, Pa.)*, vol. 37, no. 7, p. 1220, 2017.

[2] S. Yang, J. N. Martel, L. A. Lobes Jr, and C. N. Riviere, "Techniques for robot-aided intraocular surgery using monocular vision," *The International Journal of Robotics Research*, vol. 37, no. 8, pp. 931–952, 2018.

[3] H. Liao, M. Noguchi, T. Maruyama, Y. Muragaki, E. Kobayashi, H. Iseki, and I. Sakuma, "An integrated diagnosis and therapeutic system using intra-operative 5-aminolevulinic-acid-induced fluorescence guided robotic laser ablation for precision neurosurgery," *Medical image analysis*, vol. 16, no. 3, pp. 754–766, 2012.

[4] W. A. Ross, W. M. Hill, K. B. Hoang, A. S. Laarakker, B. P. Mann, and P. J. Codd, "Automating neurosurgical tumor resection surgery: Volumetric laser ablation of cadaveric porcine brain with integrated surface mapping," *Lasers in surgery and medicine*, vol. 50, no. 10, pp. 1017–1024, 2018.

[5] V. Penza, D. Salerno, A. Acemoglu, J. Ortiz, and L. S. Mattos, "Hybrid visual servoing for autonomous robotic laser tattoo removal," in *2019 IEEE/RSJ International Conference on Intelligent Robots and Systems (IROS)*. IEEE, 2019, pp. 4461–4466.

[6] M. Tucker, G. Ma, W. Ross, D. M. Buckland, and P. J. Codd, "Creation of an automated fluorescence guided tumor ablation system," *IEEE Journal of Translational Engineering in Health and Medicine*, vol. 9, pp. 1–9, 2021.

[7] W. Hill, "The tumorcnc: Development and evaluation of a first-prototype automated tumor resection device," Ph.D. dissertation, Duke University, 2016.

[8] B. Yang, M. Lange, A. Millett-Sikking, X. Zhao, J. Bragantini, S. VijayKumar, M. Kamb, R. Gómez-Sjöberg, A. C. Solak, W. Wang, *et al.*, "Daxi—high-resolution, large imaging volume and multi-view single-objective light-sheet microscopy," *Nature methods*, vol. 19, no. 4, pp. 461–469, 2022.

[9] M. Draelos, P. Ortiz, R. Qian, C. Viehland, R. McNabb, K. Hauser, A. N. Kuo, and J. A. Izatt, "Contactless optical coherence tomography of the eyes of freestanding individuals with a robotic scanner," *Nature biomedical engineering*, vol. 5, no. 7, pp. 726–736, 2021.

[10] J. Burgner, M. Müller, J. Raczkowsky, and H. Wörn, "Ex vivo accuracy evaluation for robot assisted laser bone ablation," *The International Journal of Medical Robotics and Computer Assisted Surgery*, vol. 6, no. 4, pp. 489–500, 2010.

[11] A. Acemoglu, D. Pucci, and L. S. Mattos, "Design and control of a magnetic laser scanner for endoscopic microsurgeries," *IEEE/ASME Transactions on Mechatronics*, vol. 24, no. 2, pp. 527–537, 2019.

[12] H. Mo, R. Wei, B. Ouyang, L. Xing, Y. Shan, Y. Liu, and D. Sun, "Control of a flexible continuum manipulator for laser beam steering," *IEEE Robotics and Automation Letters*, vol. 6, no. 2, pp. 1074–1081, 2021.

[13] D. Kundrat, A. Schoob, T. Piskon, R. Grässlin, P. J. Schuler, T. K. Hoffmann, L. A. Kahrs, and T. Ortmaier, "Toward assistive technologies for focus adjustment in teleoperated robotic non-contact laser surgery," *IEEE Transactions on medical robotics and bionics*, vol. 1, no. 3, pp. 145–157, 2019.

[14] M. Zhao, T. J. O. Vrielink, A. A. Kogkas, M. S. Runciman, D. S. Elson, and G. P. Mylonas, "Laryngotors: A novel cable-driven parallel robotic system for transoral laser phonosurgery," *IEEE Robotics and Automation Letters*, vol. 5, no. 2, pp. 1516–1523, 2020.

[15] P. A. York, R. Peña, D. Kent, and R. J. Wood, "Microrobotic laser steering for minimally invasive surgery," *Science Robotics*, vol. 6, no. 50, p. eabd5476, 2021.

[16] L. S. Mattos, M. Dellepiane, and D. G. Caldwell, "Next-generation micromanipulator for computer-assisted laser phonomicrosurgery," in *2011 Annual International Conference of the IEEE Engineering in Medicine and Biology Society*. IEEE, 2011, pp. 4555–4559.

[17] J. Lee, N. Deshpande, D. G. Caldwell, and L. S. Mattos, "Microscale precision control of a computer-assisted transoral laser microsurgery system," *IEEE/ASME Transactions on Mechatronics*, vol. 25, no. 2, pp. 604–615, 2020.

[18] G. Dagnino, L. S. Mattos, and D. G. Caldwell, "A vision-based system for fast and accurate laser scanning in robot-assisted phonomicrosurgery," *International journal of computer assisted radiology and surgery*, vol. 10, no. 2, pp. 217–229, 2015.

[19] S. A. Boppart, J. Herrmann, C. Pitris, D. L. Stamper, M. E. Brezinski, and J. G. Fujimoto, "High-resolution optical coherence tomography-guided laser ablation of surgical tissue," *Journal of Surgical Research*, vol. 82, no. 2, pp. 275–284, 1999.

[20] V. Mazlin, P. Xiao, J. Scholler, K. Irsch, K. Grieve, M. Fink, and A. C. Boccara, "Real-time non-contact cellular imaging and angiography of human cornea and limbus with common-path full-field/sd oct," *Nature communications*, vol. 11, no. 1, pp. 1–14, 2020.

[21] L. S. Mattos, A. Acemoglu, A. Geraldes, A. Laborai, A. Schoob, B. Tamadazte, B. Davies, B. Wacogne, C. Pieralli, C. Barbalata, *et al.*, "μralp and beyond: Micro-technologies and systems for robot-assisted endoscopic laser microsurgery," *Frontiers in Robotics and AI*, vol. 8, p. 664655, 2021.

[22] M. J. Gerber, M. Pettenkofer, and J.-P. Hubschman, "Advanced robotic surgical systems in ophthalmology," *Eye*, vol. 34, no. 9, pp. 1554–1562, 2020.

[23] M. Katz, *Introduction to geometrical optics*. World Scientific Publishing Company, 2002.

[24] X. Li, W. Zhang, W. Y. Wang, X. Wu, Y. Li, X. Tan, D. L. Matera, B. M. Baker, Y. M. Paulus, X. Fan, *et al.*, "Optical coherence tomography and fluorescence microscopy dual-modality imaging for in vivo single-cell tracking with nanowire lasers," *Biomedical Optics Express*, vol. 11, no. 7, pp. 3659–3672, 2020.

[25] Y. Fan, B. Zhang, W. Chang, X. Zhang, and H. Liao, "A novel integration of spectral-domain optical-coherence-tomography and laser-ablation system for precision treatment," *International journal of computer assisted radiology and surgery*, vol. 13, no. 3, pp. 411–423, 2018.

[26] W. Huang, C. Gao, Y. Lan, S. Zeng, J. L. Pathak, M. Zhou, L. Ge, and J. Zhang, "Optical coherence tomography characterizes the roughness and thickness of the heterogeneous layer on cortical bone surface induced by er: Yag laser ablation at different moisture contents," *Quantitative imaging in medicine and surgery*, vol. 10, no. 3, p. 713, 2020.

[27] Y. Li and J. Katz, "Laser beam scanning by rotary mirrors. i. modeling mirror-scanning devices," *Applied optics*, vol. 34, no. 28, pp. 6403–6416, 1995.

[28] P. Eisert, K. Polthier, and J. Hornegger, "A mathematical model and calibration procedure for galvanometric laser scanning systems," in *Vision, Modeling, and Visualization*, 2011, pp. 207–214.

[29] R. Y. Tsai, R. K. Lenz, *et al.*, "A new technique for fully autonomous and efficient 3 d robotics hand/eye calibration," *IEEE Transactions on robotics and automation*, vol. 5, no. 3, pp. 345–358, 1989.

[30] H. C. Lee, N. E. Pacheco, L. Fichera, and S. Russo, "When the end effector is a laser: A review of robotics in laser surgery," *Advanced Intelligent Systems*, vol. 4, no. 10, p. 2200130, 2022.